Glioma invasion and its interplay with the nervous tissue: a multiscale model

Martina Conte*[1], Luca Gerardo-Giorda[1], and Maria Groppi[2]

[1] *BCAM - Basque Center for Applied Mathematics*
Alameda de Mazarredo, 14 - E-48009 Bilbao, Spain

[2] *Dipartimento di Scienze Matematiche, Fisiche e Informatiche, Universitá di Parma*
Parco Area delle Scienze, 7/A - 43124 Parma, Italy

Abstract

A multiscale mathematical model for glioma cell migration and proliferation is proposed, taking into account a possible therapeutic approach. Starting with the description of processes taking place on the subcellular level, the equation for the mesoscopic level is formulated and, thus, the macroscopic model is derived, using a parabolic limit and the Hilbert expansions in the moment system.
After the model set up and the study of the well-posedness of this macroscopic setting, we investigate the functions involved in the equations that highlight the role of the fibers in the tumor dynamics. In particular, we focus on the fiber density function, with the aim of comparing different possible choices present in literature and understanding which approach could better describe the actual fiber density and orientation. Finally some numerical simulations, based on real data, show the role of each modelled process in the evolution of the solution.

Keyworks— Multiscale glioma modelling, Diffusion tensor imaging, Fiber distribution function, Anisotropic diffusion, Tumor response to therapy

1 Introduction

Gliomas are the most frequent types of primary brain tumors, arising from mutations of glial cells of the central nervous system. They can be classified by cell type and they are rarely curable, especially the most aggressive subtype called *Glioblastoma multiforme (GBM)*, characterized by poor prognosis and a median survival rate that rises up to 15-16 months with a standard treatment protocol [1]. A common approach for glioma includes surgical resection of the tumor mass followed by a combination of chemotherapy and radiation treatment. For what concerns the surgical procedure, a complete resection, unfortunately, is often impossible: the highly infiltrative nature of the tumor cells, in fact, leads to strong anisotropic spread, with heterogenous and often disconnected finger-like patterns, and to an 'invisible' tumor outer border, undetectable with the current medical imaging techniques. Hence, the motivations for a deeper understanding of tumor migration and invasion phenomena naturally emerge to face these issues.

The invasion of glioma cells in the human brain tissue is a highly complex phenomenon that involves several processes at different spatial and temporal scales. From the microscale, with the intracellular dynamics, through the intercellular level, where the individual cell behaviours are represented, up to the macroscopic setting for the cell population density description. The exact causes of these events are still not completely well understood and this failure is due to their complex biology at the cellular and molecular level, as well as at the level of the interactions with the surrounding environment.
Cell interactions with extra-cellular matrix (ECM) and with adjacent cells, together with biochemical processes, support the active cell movement, that occurs along preexisting brain structures, with notable preference for myelinated fibers, blood vessels and white matter tracts. In particular, in the haptotactic movement, the role of glioma cell surface receptors, such as some types of integrins [2, 3], is of great importance. Their interactions with ECM components support cells adhesion, spread and migration through the extra-cellular environment, influencing also cells growth, division and proliferation [4, 5].

*Corresponding author: mconte@bcamath.org

The role of the highly anisotropic structures of the underlying nervous tissue, influencing tumor position, shape and extent in the brain, is highlighted by instruments for medical imaging and data collection, such as Magnetic Resonance Imaging (MRI) technique, together with Diffusion Tensor Imaging (DTI) for the description of tissue anisotropy.
MRI is useful, in general, to obtain morphological information and microscopic reconstruction of the brain, due to its strong contrast between fluid and more solid anatomical structures. Even though it is not able to show completely the tumor infiltration in the tissue, it is mainly used for firstly detecting brain tumors and, then, following up their evolution.
DTI is a special kind of diffusion-weighted magnetic resonance imaging (DWI) that allows to map water molecule diffusion patterns, revealing microscopic details about tissue architecture. The detected differences in the molecular mobility describe the anisotropic effects, reflecting the peculiar physical arrangement of the medium and the presence of obstacles or promoters for the movement. The DTI method is a high value tool in the glioma prognosis, since it provides information about the local tissue structure [64], identifying aligned structures along which cell migration is more keen to occur.

Mathematical modelling of tumor cell migration and invasion inside the tissue and, in particular, the modelling of GBM growth, evolution and treatment, has evolved significantly over the past years and several different approaches have been developed and exhaustive reviewed in [6, 7, 8]. The classes of models used for the description of glioma evolution range from discrete and hybrid settings up to continuum models for the cell density. In particular, *discrete models* are used for the description of individual cells dynamics moving on a lattice (see e.g. [9, 10] and the references therein), while *hybrid models* involve both discrete and continuous equations, where the formers characterize cell motion, while the latters the evolution of external factors (see e.g., [11, 12, 13]).
In the framework of continuum equations, a significant number of studies makes use of reaction-diffusion equations to characterize glioma density directly at a macroscopic scale. Starting from the work of Swanson et al. [14] where the idea of heterogenous diffusion coefficients (two different constants for the description of the diffusion process in grey and white matter) and anisotropic diffusion has been introduced, a critical point has concerned the matching of the model to clinical data, in order to select and estimate the parameters related to tumor diffusion. A step forward in this direction has been given by connecting the tensor describing tumor diffusion with the information provided by DTI and using them in the context of mathematical modelling (see e.g. [15, 17, 18]).
Further *macroscopic models* for tumor migration rely on *mass conservation* (see e.g. [19, 20, 21, 22, 23]) and/or on *mechanical-chemical description*. The latter takes into account the forces exerted inside the tumor and at the interface between healthy and neoplastic tissue and the relevant deformation effects [16, 17, 24, 25, 26].
Multhiphase models have been developed based on mixtures modelling, where the tumor description considers the malignant mass as a saturated medium, with at least one liquid phase (e.g. water) and one solid phase (e.g. glioma cells, ECM, etc.). Examples of this approach can be found in [27, 28, 29, 30] and the references therein.
A different approach consists in deducing the macroscopic model from a mesoscopic level of description of individual cell behaviour. These models use Boltzmann-type equations for the cell population density, where the usual collision operator describes the cell velocity changes. The kinetic transport equation for the glioma cell density, in fact, does not depend on time and space only, but also on the velocity variable; a scaling argument is then used to derive the macroscopic setting [32, 31, 57, 33, 34].
This approach has been extended in order to enhance the accuracy of the models with respect to reality, connecting the modelling of subcellular processes with the mesoscopic population-level description. This has been done within the *multiscale modelling* framework, in which the information given at the subcellular level introduces additional terms to the mesoscopic and, consequently, to the macroscopic equations. In particular, this approach has been used to provide a more detailed description of the migration process, involving the cellular receptor dynamics, as described in [38, 39, 35, 40], with a special focus on the case of glioma evolution [42, 36, 37].

In our model we consider this last multiscale framework, modelling the growth and spread of glioma cells inside the brain tissue and highlighting the influence of the underlying nervous fibers on the tumor evolution. In particular, we focus on how the information about the fiber structures, coming from the clinical data, are translated and encoded in the model in order to achieve a more realistic description of glioma cell spread and migration. Moreover, the role of these processes that characterize glioma evolution is investigated.
The three different scales characterizing the processes and the model setting follow a well-established modelling approach. On the *microscale*, as firstly proposed for the specific case of glioma in [36], we account for processes taking place on the subcellular level, concerning the dynamics of bound receptors on the cellular membrane and described by an ODE for the mass action kinetics. On the *mesoscale*, we analyze the individual cell behaviors involving the interactions with the surrounding tissue, whose anisotropic characteristics are accurately taken into account, as well as the proliferation process and the modelling of a standard therapeutic treatment. In particular, following the idea of [37], according to the general setting proposed in [33, 43], proliferation is included in the model as a result of cell-tissue interactions, while, for the treatment, mainly refering to [41], a

combination of chemo- and radio-therapy is considered (see also e.g.[44, 45, 46] and references therein). Finally, the *macroscopic* setting is derived from a parabolic scaling of the mesoscopic equation, as previously done in [42, 36, 37, 41], leading to an evolution equation for the macroscopic cell density.
Together with this specific modelling approach, the role of the fiber is enhanced by a novel and comprehensive comparison of the functions, presented in literature, for the fiber description. In particular, this comparison, as well as the numerical simulations of the macroscopic model, has been done considering real DTI data on a reconstructed real geometry of a slice of brain.

This work is organized as follow. In Section 2 we describe the different processes and scales involved in the model, providing a formal derivation of the macroscopic setting and proving its well-posedness. Section 3 is dedicated to the analysis of the fiber distribution function that represents the connection between the diffusion tensor involved into the equations and the information provided by the MRI and DTI data (enabling their integration inside the model). In Section 4 different numerical simulations showing the dynamics of glioma cells in different scenarios are presented: first, the different fiber distribution functions described in Section 3 are tested to observe their effect on tumor evolution; then, we focus specifically on the role of the subcellular dynamics; finally, we discuss the effect of the two specific treatments on tumor density. In the last Section 5 we comment on the main results of the model and its performance, together with few concluding remarks.

2 The model

Here we combine two different approaches, mainly presented in [37] in terms of model set up and proliferation term description and in [41] for the therapy description. We define a setting that starts from a description of cell receptor dynamics on the microscale and, adding the description of a possible therapeutic approach, leads to an advection-diffusion-reaction equations on the macroscale.

2.1 Cellular level

On this level we focus on the microscopic cell surface receptor dynamics. With the aim of understanding its influence on the macroscopic movement behaviour at the tissue scale, we consider some transmembrane adhesion proteins that bind to unsoluble proteins in the underlying brain ECM. The concentration of bounded receptors is denoted by $y(t)$ and we assume that this binding occurs preferentially in regions of highly aligned tissue.

Starting from to the description introduced in [36] and in [41] and to which we refer for further details, for readers convenience we recall here the main peculiarity of the microscopic setting. The mass action kinetics for the concentration $y(t)$ is described by the following ordinary differential equation:

$$\dot{y} = k^+(d_c)(1-y)Q(x)S(\alpha_2, d_r) - k^-(d_c)y\,. \tag{1}$$

In this equation $Q(x)$ indicates the volume fraction of tissue and includes ECM components and the myelinated brain fibers. Moreover, the therapy modelling appears through the terms S, k^+ and k^-. As in [47, 41], the chemotherapeutic treatment, whose dose is denoted by d_c, is aimed to reduce cell invasion, influencing the interactions between cell receptors and ECM, through the dependence of the attachment and detachment rates $k^+(d_c)$ and $k^-(d_c)$ from d_c, and to make the cancer cells more sensitive to radiotherapy. This latter, instead, is directly aimed at the cell killing and its dose is denoted by d_r. In particular, d_c and d_r are at least piecewise time-dependent functions.
In the line of the well-estabilished linear-quadratic radiobiological model (L-Q) [48], the surviving fraction of cells post radiotherapy is described by

$$S(\alpha, d) = exp(-\alpha d - \beta d^2)\,. \tag{2}$$

From now on, we use different values for the parameters α and β for the tumor cells and the normal tissue: in particular, α_1 and β_1 refer to glioma cells, while α_2 and β_2 to the healthy ones.

Since the microscopic cell surface receptor dynamic is assumed to be much faster than the macroscopic time scale and, then, equilibrates rapidly [37], we consider the unique steady state y^* of the equation (1):

$$y^* = \frac{k^+(d_c)Q(x)S(\alpha_2, d_r)}{k^+(d_c)Q(x)S(\alpha_2, d_r) + k^-(d_c)} =: f(k^+(d_c), k^-(d_c), Q(x), S(\alpha_2, d_r))\,. \tag{3}$$

Introducing a new internal variable $z := y^* - y$, that measures the deviation from the steady state, we consider the path of a single cell starting in x_0 and moving with velocity v through a time-invariant density field $Q(x)$.

With the notation $x = x_0 + vt$, it is possible to redefine (1) as a new equation for the deviation $z(t)$ having the following form [41]:

$$\dot{z} = -z(t)(QSk^+ + k^-) + F(t) + f'(Q)v \cdot \nabla Q =: G(z, Q, d_c, d_r) \tag{4}$$

where

$$F(t) := \dot{d}_c\Big(\frac{\partial f}{\partial k^+}(k^+)'(d_c) + \frac{\partial f}{\partial k^-}(k^-)'(d_c)\Big) + \dot{d}_r f'(S)S'(d_r)\,. \tag{5}$$

2.2 Intercellular level

Using the above description of the microscopic dynamics, we describe the cell behavior with the aid of velocity-jump processes. Starting from the model setting proposed in [37], to which we refer for further details, and including also the radio-therapy description as above, we present here and describe the resulting equation. We consider the glioma density function $\rho(t, x, v, z)$ at time t, position $x \in \mathbb{R}^n$, velocity $v \in V \subset \mathbb{R}^n$, and internal state $z \in Z \subseteq [y^* - 1, y^*] \subset \mathbb{R}$; the kinetic transport equation for its dynamic is given by:

$$\partial_t \rho + \nabla_x \cdot (v\rho) - \partial_z\big[G(z, Q, d_c, d_r)\rho\big] = \mathcal{L}[\lambda]\rho + P(\rho) - L(\bar{\rho}, \alpha_1, d_r)\rho\,. \tag{6}$$

Here, $\mathcal{L}[\lambda]\rho$ denotes the turning operator, a mathematical representation of the cell velocity changes. They are due, in particular, to contact guidance, that describes the oriented motility response of cells to anisotropy of the environment. In the case of glioma cells the movement and spread are especially related to white matter tracts, used as highways for their migration movement. $\mathcal{L}[\lambda]\rho$ is defined via an integral operator of Boltzmann type [57]

$$\mathcal{L}[\lambda]\rho = -\lambda(z)\rho + \lambda(z)\int_V K(x, v)\rho(v')dv' \tag{7}$$

where $\lambda(z) := \lambda_0 - \lambda_1 z$ is the turning rate, depending on the amount of bound integrins, with λ_0 and λ_1 positive constants. The term $\lambda(z)\rho$ gives the rate at which cells switch away from velocity v. The integral term denotes the cell switching into velocity v from all other velocities.
In order to model the turning kernel $K(x, v)$ in (7) we assume that the dominating directional cue is given by the oriented environment of the brain fibers and, consequently, cells choose their new direction according to the given fiber network. We describe the oriented structure of the environment by defining a directional distribution $q(x, \hat{v})$, with $\hat{v} \in \mathbb{S}^{n-1}$ and with symmetry $q(x, \hat{v}) = q(x, -\hat{v})$. In this framework, assuming a constant cell speed, i.e. $V = s\mathbb{S}^{n-1}$, the turning kernel is modelled as $K(x, v) = \frac{q(x,\hat{v})}{\omega}$, with scaling costant $\omega := \int_V q(\hat{v})dv = s^{n-1}$ [57, 36].
In addition, if we indicate as integrin activation the binding to the tissue, we regard to it as the onset of proliferation and reorientation: in fact the turning rate of the cells depends on the receptor state. In particular, if many receptors are already bound, then the rate $\lambda(z)$ is expected to increase, since in that case the cells will need to change their direction more often in order to make them "free" from the too densely packed fibers surrounding them [49].
For the proliferation term $P(\rho)$ in (6), as in [37], we consider the so-called proliferative interactions, modeled as a product between the mesoscopic glioma density ρ and the volume fraction of brain tissue Q:

$$P(\rho) = \mu(x, \bar{\rho}, v)\int_Z \chi(x, z, z')\rho(t, x, v, z')Q(x)dz' \tag{8}$$

where $\bar{\rho} = \bar{\rho}(t, x)$ is defined by $\bar{\rho}(t, x) = \int_V \int_Z \rho(t, x, v, z)dvdz$ and $\mu(x, \bar{\rho}, v)$ denotes the growth rate. In the integral operator, the kernel $\chi(x, z, z')$ characterizes the transition from the state z' to the state z during the proliferative process at position x. No particular conditions are required on χ, we only assume that the nonlinear proliferative operator $P(\rho)$ is uniformly bounded in the L^2-norm, a reasonable biological condition linked to the space-imposed bounds on the cell division.
The last term in (6), the death term, results as a combination of two parts: the term related to the natural death of the cells and that one related to the radio- therapy:

$$L(\bar{\rho}, \alpha_1, d_r)\rho = (l(\bar{\rho}) + R(\alpha_1, d_r))\rho\,. \tag{9}$$

In particular, in the real clinical practice, the total dose of drug d_r is given in small fractions, in order to avoid toxic effects to normal tissue. If ν is the number of fractions, it is possible to collect the effects of the radiation treatment protocol into the following term:

$$R(\alpha, d_r) = \sum_{i=1}^{\nu}(1 - S(\alpha, d_r))\eta_\delta(t - t_i) \tag{10}$$

where η_δ is a C_0^∞ function with unit mass and support in $(-\delta, \delta)$, $\delta \ll 1$ and t_i, varying i, denote the time instants at which a ionizing radiation is applied to the patient.

Equation 6 follows the line proposed in [38] and global existence of a unique solution can be proved as in [38], under some proper growth conditions for μ with respect to its third argument v. The next step will be the derivation of the macroscopic equation for the macroscopic cell population density.

2.3 Scaling of the mesoscopic equation

Considering the above analysis for the dynamics on the cellular and intercellular level, we start from the obtained evolutionary equation (6) for the density $\rho(t, x, v, z)$. We introduce proper scaling arguments in order to deduce the macroscopic density equation, following [36, 37, 41], where we refer to for further details. Let us here recall the main aspects, introducing the moments

$$\begin{aligned} m(t,x,v) &= \int_Z \rho(t,x,v,z)dz & M(t,x) &= \int_V m(t,x,v)dv \ (= \bar{\rho}(t,x)) \\ m^z(t,x,v) &= \int_Z z\rho(t,x,v,z)dz & M^z(t,x) &= \int_V m^z(t,x,v)dv\,. \end{aligned} \tag{11}$$

We do not consider higher order moments of ρ, in virtue of the fact that the subcellular dynamic is much faster than the events on the higher scales, so the deviation z is close to zero. To perform the following calculations we also assume the data to be compactly supported in the phase space $< x, v, z >$.
We integrate equation (6) with respect to z twice, once pre-multiplying it by z. Then we use a parabolic scaling $\hat{x} \to \epsilon x$ and $\hat{t} \to \epsilon^2 t$ for the time and space variables respectively. In particular, the quantity $F(t)$, that involves time derivatives of the different doses, d_c and d_r, and of the cell survival fraction S and accounts for fast dynamics, is scaled with ϵ^2, as well as the proliferation rate $\mu(x, M, v)$, to let it act on the correct new time scale, and the loss term $L(M, \alpha_1, d_r)$.
Therefore, dropping hats, the following equations are obtained:

$$\begin{aligned} &\epsilon^2\partial_t m + \epsilon\nabla_x\cdot(vm) = -\lambda_0 m + \lambda_0\frac{q}{\omega}M + \lambda_1 m^z - \lambda_1\frac{q}{\omega}M^z \\ &+\epsilon^2\mu(x,M,v)\int_Z\int_Z \chi(x,z,z')\rho(t,x,v,z')Q(x)dz'dz - \epsilon^2 L(M,\alpha_1,d_r)m \end{aligned} \tag{12}$$

$$\begin{aligned} &\epsilon^2\partial_t m^z + \epsilon\nabla_x\cdot(vm^z) = -m^z(QSk^+ + k^-) + \epsilon^2 F(t)m + \epsilon f'(Q)v\cdot\nabla_x Q\, m + \\ &-\lambda_0 m^z + \lambda_0\frac{q}{\omega}M^z + \epsilon^2\mu(x,M,v)\int_Z\int_Z z\chi(x,z,z')\rho(t,x,v,z')Q(x)dz'dz + \\ &-\epsilon^2 L(M,\alpha_1,d_r)m^z\,. \end{aligned} \tag{13}$$

Now, applying the asymptotic Hilbert expansions of the moments of ρ [34, 50] and collecting the coefficients of the different powers of ϵ in equations (12) and (13), we obtain, at leading order, $M_0^z = 0$, $m_0^z = 0$ and $m_0 = \frac{q}{\omega}M_0$. Then, from these results, we get $M_1^z = 0$ and, using compactness properties, it is possible to deduce $M_1 = 0$ and

$$m_1 = \frac{1}{\lambda_0}\Big[\frac{\lambda_1}{\lambda_0 + k^+QS + k^-}f'(Q)\nabla Q\cdot v\frac{q}{\omega}M_0 - \nabla_x(v\frac{q}{\omega}M_0)\Big]\,. \tag{14}$$

Finally, considering (14) and plugging it into the equation for ϵ^2 and integrating it with respect to v, we obtain the following simplified form for the evolution equation for the macroscopic glioma density M_0:

$$\begin{aligned} &\partial_t M_0 - \nabla\cdot(D_T(x)\nabla M_0) + \nabla\cdot((g(Q(x))D_T(x)\nabla Q - u(x))M_0) = \\ &= \mu(x,M_0)Q(x)M_0 - L(M_0,\alpha_1,d_r)M_0\,. \end{aligned} \tag{15}$$

In particular, here we assume μ, the growth rate, not to explicitly depend on v, while

$$g(Q(x)) := \frac{\lambda_1}{\lambda_0 + k^+QS + k^-}f'(Q)$$

indicates the function carrying the information about the influence of the subcellular dynamics of receptor bindings.
The macroscopic diffusion tensor is denoted by

$$D_T(x) := \frac{1}{\omega\lambda_0}\int_V v \otimes v\, q(x,\hat{v})dv \tag{16}$$

and the tumor drift velocity is given by

$$u(x) := \frac{1}{\omega\lambda_0}\int_V v \otimes v\, \nabla q(x,\hat{v})\, dv\,. \tag{17}$$

It is important to stress that, even though the similarity between the macroscopic setting proposed in [37] and equation (15) are evident, there are substantial differences, due to the modelling of the therapeutic approach, introduced in [41], in this setting. More precisely, therapy is not only present in the term $L(M_0, \alpha_1, d_r)$, but also the influence of both chemo- and radio-therapy is hidden inside the function $g(Q(x))$ in the drift term.

2.4 Well-posedness of the macroscopic setting

Using the theory of monotone operators for non-linear parabolic equations and following a well-known framework [51, 52], it is possible to prove existence, uniqueness and non-negativity of the solution of the parabolic problem (15) with Neumann boundary conditions.
Let $\Omega \subset \mathbb{R}^3$ a bounded domain with $\partial\Omega \in C^{0,1}$, i.e. Ω is a Lipschitz domain. Set a finite $T > 0$, we consider the following non-linear parabolic initial boundary value problem related to equation (15):

$$\begin{cases} \partial_t M - \nabla\cdot(D_T(x)\nabla M) + \nabla\cdot(Y(Q,D_T)M) + \Gamma(M) = 0 \quad \text{in } [0,T]\times\Omega \\ \nabla M\cdot\mathbf{n} = 0 \quad \text{on } [0,T]\times\partial\Omega \\ M(0,x) = M_0(x) \quad \text{in } \Omega \end{cases} \tag{18}$$

where

$$\begin{aligned} Y(Q,D_T) &= g(Q(x))D_T(x)\nabla Q \,-\, u(x) \\ \Gamma(M) &= ((l(M) + R(\alpha_1,d_r)) - \mu(x,M)Q(x))M\,. \end{aligned} \tag{19}$$

Adapting the proof proposed in Appendix A.1 of [37], it is possible to prove the following theorem.

Theorem. *Under the following main assumptions:*

- *A.1 The tensor $D_T(x)$ is uniformly positive definite, it lies in the space $W^{1,\infty}(\Omega)$ and its smallest eigenvalue is larger than a constant $\alpha > 0$;*
- *A.2 $\Gamma(M)$ is continuous w.r.t. time and M and it satisfies the growth condition $|\Gamma(s)| \le c\,(1+|s|^{r-1})$ for some $r \ge 1$, with a constant c independent of time and space, and the coercivity condition $\inf_{s\in\mathbb{R}^+}\Gamma(s)s > -\infty$;*
- *A.3 The volume fraction of tissue fibers $Q(x)$ lies in the space $W^{1,\infty}(\Omega)$;*
- *A.4 The rates k^+ and k^- are continuous in the variable d_c (which has to be continuous in time) and uniformly bounded;*
- *A.5 The overall term $Y(Q,D_T)$ is in $L^\infty(\Omega)$.*

Let set $U = H^1(\Omega)$, $H = L^2(\Omega)$ and $X = L^2(0,T;H^1(\Omega))$ and define for all $M,\varphi \in X$ the operators:

$$\begin{aligned} \langle A_1 M,\varphi\rangle_X &:= \int_0^T\int_\Omega [D_T\nabla M - M\cdot Y(Q,D_t)]\nabla\varphi dxdt \\ &= \langle AM,\varphi\rangle_X + \left\langle \tilde{A}M,\varphi\right\rangle_X \end{aligned} \tag{20}$$

$$\langle A_2 M,\varphi\rangle_X := \int_0^T\int_\Omega \Gamma(M)\varphi dxdt \tag{21}$$

and the functional space W defined as:

$$W := \{\omega \in L^2(0,T;H^1(\Omega)) \,:\, \omega_t \in L^2(0,T;(H^1(\Omega))^*)\} \subseteq X\,.$$

Let $M_0 \in L^2(\Omega)$ and $\Gamma : \mathbb{R} \to \mathbb{R}$ a continous function that satisfies the above conditions with $1 \leq r < \frac{10}{3}$. Then there exists a weak solution $M \in W$ of the problem (18), i.e. for all $\varphi \in C_0^\infty([0,T] \times \Omega)$:

$$\int_0^T \langle \partial M_t, \varphi \rangle_{H^1(\Omega)} \, dt + \int_0^T \int_\Omega (D_T \nabla M - Y(Q, D_T) M) \nabla \varphi dx dt + \int_0^T \int_\Omega \Gamma(M) \varphi dx dt = 0$$

or, equivalently,

$$- \int_0^T \left\langle M(t), \varphi'(t) \right\rangle_{H^1(\Omega)} dt + \int_0^T \left\langle (\tilde{A}_1 + A_2) M(t), \varphi(t) \right\rangle_{H^1(\Omega)} dt = \langle M_0, \varphi(0) \rangle_{L^2(\Omega)} \, .$$

It is also possible to prove uniqueness and non-negativeness of the solution, using classical estimates, parabolic comparison principle [53] and theorems from Section III.4.1. in [52].

Proposition 1. *The solution of the macroscopic problem (18) is unique if $\Gamma(M)$ is strictly monotone. In addition, if $M_0 \geq 0$, the solution of (18) is nonnegative.*

3 Fiber Distribution Function

The analysis of the connection between the external data introduced in the model and the way in which they are processed, as well as how their features are reproduced and taken into account, is fundamental in order to obtain reliable simulations of tumor dynamics from both qualitative and quantitative point of views. Therefore, we focus our attention on the analysis of a specific term involved in the macroscopic setting (15), the *fiber distribution function* $q(x, \hat{v})$.
In particular, we investigate the way in which the information about the diffusivity in the brain and the anisotropic characteristics of the nervous tissue could be taken into account in the model.
To analyze this aspect we consider the *fractional anisotropy index* FA (see Appendix A.1 for further details) as a tool to understand and compare how the information provided by the DTI data and encoded in the water diffusion tensor D_W are translated and preserved into the model.

The fiber probability density function $q(x, \hat{v})$ represents the link between raw data, collected in the water diffusion tensor $D_W(x)$, and tumor diffusion tensor $D_T(x)$, characterising tumor movement and diffusivity in the model equation, as shown by relation (16). It is used to describe the probability density of switching to velocity $\hat{v}$, turning at point x, and it can be derived in different ways according to the chosen distribution.
Considering the different expressions used in literature for $q(x, \hat{v})$, we analyze and compare the *Peanut Distribution* [57], the *Bimodal von Mises-Fisher Distribution (VMF)* [59, 57] and the *Orientation Distribution Function (ODF)* [60], described in details in Appendix A.2, A.3 and A.4, respectively, and having the following expressions:

$$q(x, \theta) = \frac{3}{|\mathbb{S}^2| Tr \, D_W(x)} \theta^T D_W(x) \theta \qquad \text{(Peanut)} \tag{22}$$

$$q(x, \theta) = \frac{\delta}{4\pi} + (1 - \delta) \frac{k(x)}{4\pi \sinh k(x)} \left(\cosh(k(x) \phi_1 \cdot \theta) \right) \qquad \text{(Bimodal VMF)} \tag{23}$$

$$q(x, \theta) = \frac{1}{4\pi |D_W(x)|^{\frac{1}{2}}} (\theta^T (D_W(x))^{-1} \theta)^{-\frac{3}{2}} \qquad \text{(ODF)} \, . \tag{24}$$

We will highlight the specific capabilities of these different distributions to accurately reproduce the anisotropic characteristics of the underlying nervous tissue, their strengths and their weaknesses, in order to clarify their choice in the model.

3.1 Comparison of $q(x, \theta)$ on a single data point

We firstly consider a single spatial point x and we compute D_T from D_W with the three different functions $q(x, \theta)$. We assume for D_W a greater diffusion in the $y-$axis direction than in the $x-$axis one (Figure 1); by visualizing the tensors, it is possible to immediately grasp the difference between the ellipsoids and, consequently, the way they reproduce the original anisotropy.
For the Peanut distribution (22), the anisotropy showed by Figure 1 is in large part lost in the related plot of Figure 2, due to the independency from D_W of the strong isotropic component of D_T in (31). The tumor diffusion tensor D_T related to the VMF distribution (23) shows, instead, a degree of anisotropy similar to that of the original D_W. In particular this trend can be better observed for increasing values of κ or for decreasing

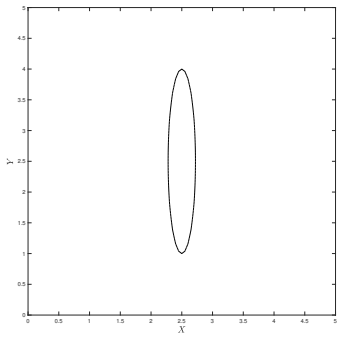

Figure 1: $D_W(x)$ in the point $\mathbf{x}$.

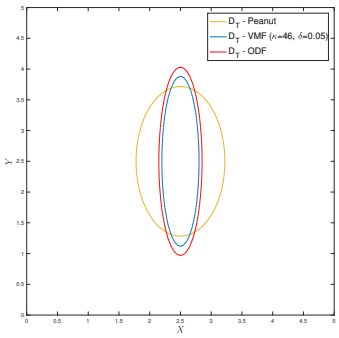

Figure 2: $D_T(x)$ in the point $\mathbf{x}$.

values of δ (see Figure 16 in Appendix).
The ODF (24), in the related plot of Figure 2, leads to similar shape and proportions between the two curves related to D_W and D_T. In particular, a greater preservation of the anisotropic characteristics with respect to the Peanut distribution case is observed and, moreover, the independence from the parameter value selection, that would involve an unclear biological estimation, gives an additional benefit with respect to the VMF distribution.

It has been proved analytically in [57] for the Peanut distribution that $FA(D_T) \leq FA(D_W)$, i.e. the resulting anisotropy of D_T results always lower than the anisotropy of the original tensor D_W. So D_T could not be able to reproduce the brain structure accurately, especially in the case of crossing fiber tracts.
For the VMF distribution, instead, formally in the limit of $\delta \to 0$ and $\kappa \to \infty$, it results $FA(D_T) \to 1$, i.e. in principle the fractional anisotropy index FA can even reach its maximum theoretical value.

3.2 Comparison on 2D slices

Here we compare the behaviour of the different fiber distribution functions (22),(23) and (24) on real DTI data. This dataset was acquired at the Hospital Galdakao-Usansolo (Galdakao, Bizkaia), and approved by its Ethics Committee: all the methods employed were in accordance to approved guidelines.
As above commented, DTI measures the apparent diffusivity of water molecules per volume element and it captures this feature using the symmetric 3D tensor D_W.
The DTI data processing is done using FSL (FMRIB Software Library)[1] [65], a comprehensive library of analysis tools for MRI and DTI brain imaging data. With FSL the information about the diffusivity, through the tensor eigenvalues and eigenvectors, are extracted and, consequently, tissue structure and anisotropy are provided.

We consider here a 2D slice obtained from an horizontal section of an entire brain DTI dataset, as it is sufficiently representative of the methodology. We compute the fractional anisotropy $FA(D_W)$ and $FA(D_T)$, obtaining the comparison shown in Figure 3 and 4.

What clearly emerges is that the use of the Peanut distribution identifies accurately the locations where the fibers are aligned or not, without significant over- or under-estimations of these areas. The main problem is related to the degree of anisotropy: in fact, the resulting tumor diffusion tensor D_T (31) shows a degree of anisotropy significantly lower, with values for the fractional anisotropy almost reduced by half in the areas of greater alignment, according to the original tensor data (Figure 3).
The use of the ODF provides a general underestimation of the degree of anisotropy, although highly improving the results of the Peanut distribution, and it preserves with sufficient accuracy the description of the location of aligned and not-aligned fibers.
For the VMF distribution the results are highly dependent on κ and δ, whose effect can be observed into more details in Figures 17 and 18 in Appendix A.3. In particular, in terms of the extension of the anisotropic regions, the VMF distribution provides an over-estimation of them, while in terms of degree of anisotropy, depending on the calibration of κ and δ, there could be an over- or an under-estimation of the real anisotropy level. Figures 4 highlights a better preservation of the FA in the case of the VMF distribution, at the price of involving parameters with an unclear biological estimation.
This affects the description of the geometry peculiarities and, thus, it could have some influence in the evolution of the tumor dynamics.

[1] Information available from https://fsl.fmrib.ox.ac.uk/fsl/fslwiki/FSL

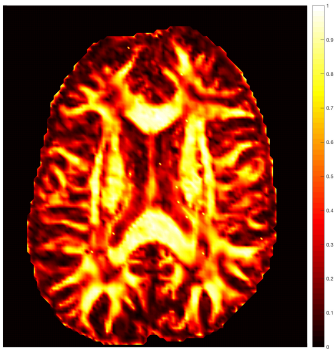

Figure 3: FA(D_W).

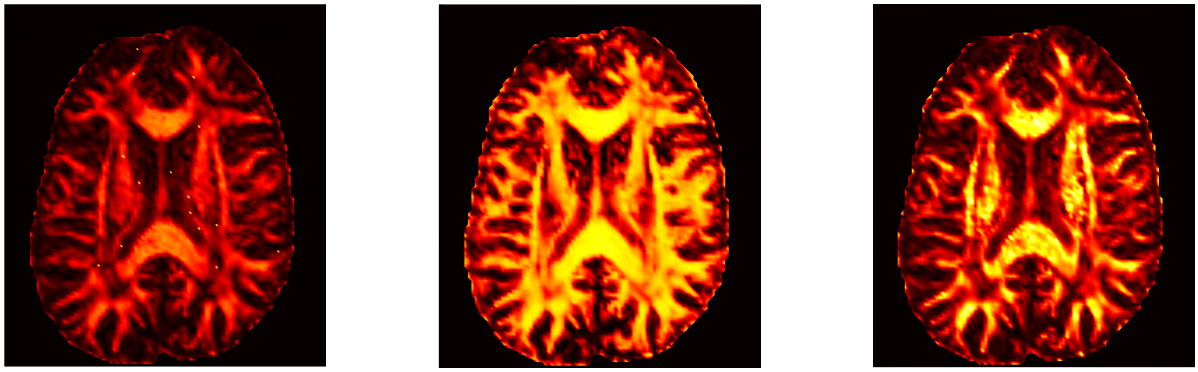

Figure 4: From left to right, FA(D_T) with Peanut distribution, VMF distribution with $\delta = 0.05$ and $\kappa = 7$ and ODF

A closer look at the peculiarities of the three distributions can be done by considering different coronal planes of this 2D slice and looking at the variation of the fractional anisotropy along the median plane. In Figure 5 the comparison between $FA(D_W)$ and $FA(D_T)$ is shown for one choice of the coronal plane.

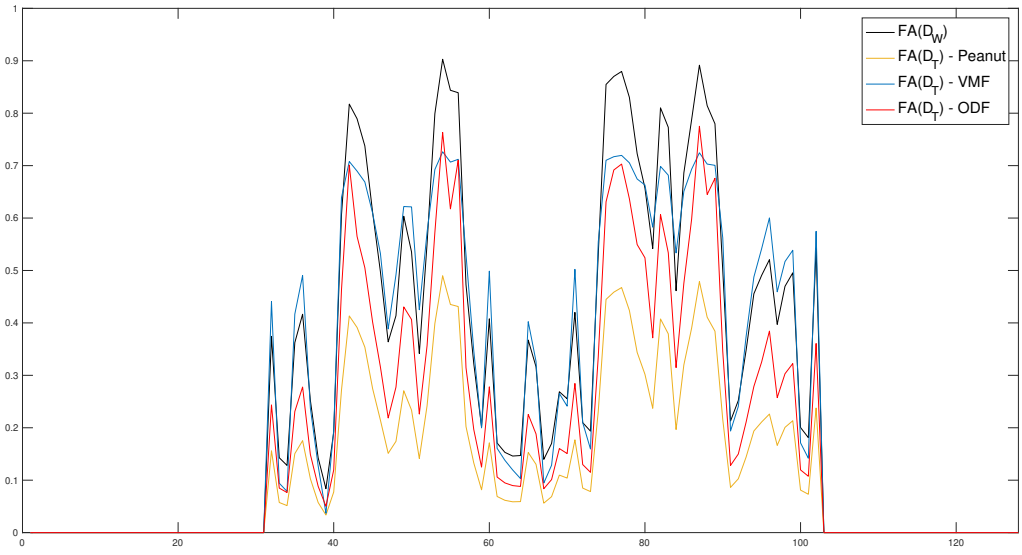

Figure 5: Comparison between FA(D_W) and FA(D_T) along the median plane of a 2D brain slice.

As it can be noticed in Figure 5, Peanut distribution and ODF have almost an identical trend, but, as expected, the Peanut distribution almost halves the degree of anisotropy with respect to the original data, while the ODF preserves it significantly better.
VMF distribution, instead, provides an under-estimation of the fractional anisotropy, when it is bigger, while

it gives an over-estimation of FA in the points in which it is smaller. Changing the considered coronal plane, the qualitative results do not change and the trend of the fractional anisotropy remains almost the same.

In order to have a more global perspective, we consider the relative difference between the FA of the original data D_W and the one related to the tumor diffusion D_T, given by the following expression:

$$R(D) = \frac{FA(D_W) - FA(D_T)}{FA(D_W)}\,. \tag{25}$$

In particular we are not considering the absolute value of the numerator in order to be able to visualize situations of both under-estimation and over-estimation of the fractional anisotropy.
In Figure 6 we firstly observe if and where the different distributions provide an over-estimation or an under-

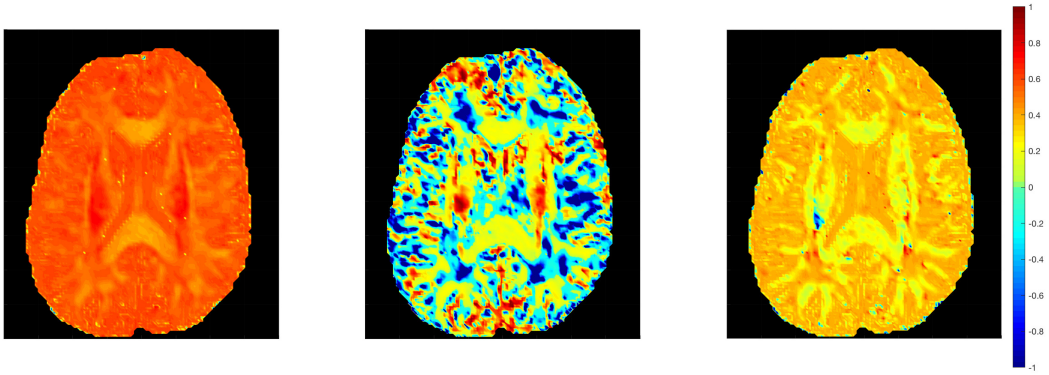

Figure 6: From left to right, R(D) for Peanut distribution, VMF distribution with $\delta = 0.05$ and $\kappa = 7$ and ODF.

estimation of $FA(D_W)$. As already briefly commented before, except for some isolated blue areas in the ODF plot - possibly related to errors in the measurements and/or to oscillation in the calculations - the VMF distribution is the only one with a mixed trend. It passes from areas of over-estimation of the anisotropy (colors from green to blue), where the values of the original FA are lower, to areas of under-estimation of FA, (colors from green to red), where there are higher values of FA(D_W).
An additional information emerging from Figure 6 is that in the highly aligned areas, where FA is bigger, the three distributions make lower average errors in estimating this value, with respect to the more isotropic regions. Moreover, in these highly anisotropic areas, this difference becomes smaller when we pass from Peanut distribution to ODF and, then, to VMF distribution. Moreover, the use of the VMF distribution must be considered with care, due to the cons highlighted above.

Furthermore, it is important also to comment about the computational cost of the three different distributions. For the Peanut distribution and the VMF distribution the computational cost for the calculation of the fiber distribution function and the resulting tumor diffusion tensor D_T is almost identical. In particular, the construction using the Peanut distribution does not require any matrix multiplication, while one matrix product is needed for the calculation of D_T in each voxel with the VMF distribution.
The ODF, instead, requires more calculations and, therefore, an higher computational cost. In fact for each voxel it requires the numerical approximation of a spherical integral, whose cost depends on the chosen numerical method. The common operations involved in the integrand function evaluation, no matter which approximation is used, involve several matrix products and a matrix inversion. Then, the cost depends on the quadrature rule. We choose the Gauss-Legendre quadrature formula and, in this case, the computational cost for the calculation of D_T in each voxel of the 3D mesh grid is $\mathcal{O}(m^2)$, where m indicates the number of points of the quadrature formula.

4 Numerical Simulations

We present 2D simulations of the resulting macroscopic advection-diffusion-reaction equation (15). The numerical simulations are performed with a self-developed code in Matlab (MathWorks Inc., Natick, MA) on the left hemisphere of a horizontal brain slice. The macroscopic tensor $D_T(x)$ si precalculated using brain data, according to the above described procedure, and the computational domain is reconstructed as explained below. A finite element scheme based on the Galerkin method for the spatial discretization is considered, together with an implicit Euler scheme for the time discretization.

4.1 Reconstruction of the computational domain

By accessing and processing data provided by MRI, it is possible to extract information about the brain geometry and structure, in order to reconstruct a realistic computational domain for the numerical simulations.
For the brain geometry processing we use the FreeSurfer Software Suite[2], an open source software for the analysis and visualization of structural and functional neuroimaging data from cross-sectional or longitudinal studies. The processing of MRI data with FreeSurfer provides surface and volume information about the two hemispheres of the brain separately, leading to the extraction of a 2D slice that constitutes our computational domain. Examples of the processed outputs are shown in Figures 7, where the entire left hemisphere surface is visualized, and 8, that shows the outer border of the considered 2D slice.

In particular a match between the voxel mesh, given by the DTI dataset, and the brain slice, coming from the

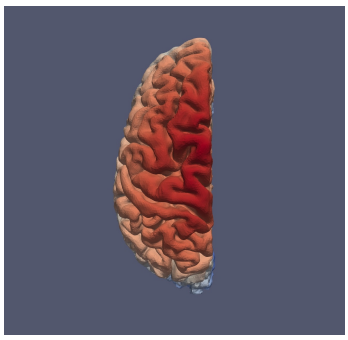

Figure 7: Left hemisphere visualized with Paraview[3]

Figure 8: Contour of one slice of the brain

processed MRI data, has been obtained with the help for different visualization softwares (e.g. Paraview and FSLeyes, the FSL image viewer). The resulting 2D domain has been triangulated with the free mesh generator Gmsh[4] and, then, the matrices of the finite element approximation have been computed.

4.2 Coefficient functions and parameters

For the volume fraction of tissue $Q(x)$, interacting at point x with the tumor population, we choose it to be proportional to the fractional anisotropy of the tissue itself. For this approach, introduced in [36], the argumentation is related to the fact that the fractional anisotropy is a measure of the alignment of the brain fibers and the volume fraction $Q(x)$ should be higher where the tissue is strongly aligned

$$Q(x) = FA(D_W(x))\,. \tag{26}$$

Other possibilities have also been considered, especially the one introduced in [42] and based on the characteristic diffusion length l_c, but no significant differences have been detected.

The growth rate $\mu(x, M_0)$ can be also chosen in different ways, especially due to the reduced availability of biological data. Following the choice made in [37, 15], we use a logistic growth term

$$\mu(x, M_0) = c_g(1 - \frac{M_0}{C_M}) \tag{27}$$

with growth rate c_g and carrying capacity C_M.

For the receptor binding rates and for the term describing the natural death of the cells, referring to the information provided in [41], we choose

$$\begin{aligned} k^+(d_c) &= 0.1\Big(1 + \frac{d_c}{1 + d_c^2}\Big) \\ k^-(d_c) &= 0.1\Big(1 + d_c\Big) \\ l(M_0) &= c_l M_0\,. \end{aligned} \tag{28}$$

[2]Information can be found in https://surfer.nmr.mgh.harvard.edu/fswiki/FreeSurferWiki and, for further details, see [69] and references therein.

[3]Open-source multiple-platform application for interactive, scientific visualization. Information available at https://www.paraview.org.

[4]Information available at http://gmsh.info and, for further details, see also [70].

The expressions for the attachment and detachment rates are in agreement with the assumption done for the chemotherapeutic term in Section 2, i.e. we consider the function k^+ monotonically decreasing with respect to the given dose d_c, while the function k^- monotonically increasing with d_c.

Eventually, in Tabel 1 we report the range of the values for the remaining parameters involved in the macroscopic equation (15).

Parameter	Value	Source
s	$0.21 \cdot 10^{-6} \frac{m}{s}$	[44]
λ_0	$0.1 \frac{1}{s}$	[66]
λ_1	$0.01 \frac{1}{s}$	[36]
c_g	$[0.32, 0.72] \times 10^{-5} \frac{1}{s}$	[67]
c_l	$[0.32, 0.72] \times 10^{-7} \frac{1}{s}$	estimated, based on [42]
C_M	≈ 1	normalized, based on [37]
α_1	$[0.018, 0.401] \frac{1}{Gy}$	[68]
α_2	$[0.373, 0.389] \frac{1}{Gy}$	[68]
β_1	$[0.023, 0.091] \frac{1}{Gy^2}$	[68]
β_2	$[0.016, 0.052] \frac{1}{Gy^2}$	[68]

Table 1: Model parameters

4.3 Results

Considering the parameters given in Table 1, we performed numerical simulations on the domain in Figure 8 for different scenarios.
In Figure 9, the value of the Fractional Anisotropy of the original water diffusion tensor $D_W(x)$ on the domain is shown. The underlying fiber structure, that highly influences the dynamics, is shown in Figure 10 by the fiber tracts in a smaller subdomain, where the leading eigenvector of the tensor $D_W(x)$ is plotted in each point x.

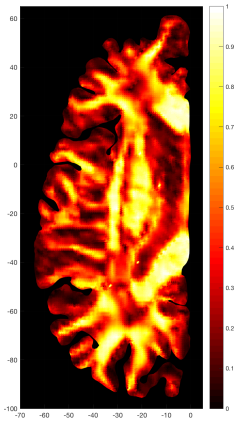

Figure 9: Fractional anisotropy of $D_W(x)$.

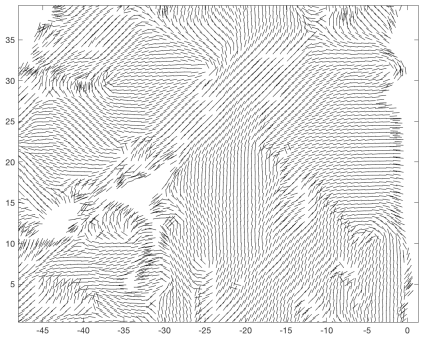

Figure 10: Visualization of the fiber tracts (zoom).

The macroscopic equation (15) we are investigating is given by

$$\begin{aligned} &\partial_t M_0 - \nabla\nabla : D_T(x) M_0 + \nabla \cdot (g(Q(x)) D_T(x) \nabla Q \, M_0) = \\ &= \mu(x, M_0) Q(x) M_0 \; - \; L(M_0, \alpha_1, d_r) M_0 \end{aligned} \tag{29}$$

with coefficient functions and parameters specified and described above. We consider homogenous Neumann boundary conditions and an initial constant tumor mass on a small portion of the domain.

We present three different series of numerical results: (A) considering the model without therapy, a comparison between the tumor evolution with the three different fiber distribution functions; (B) fixing one distribution, a comparison of this model with the one without subcellular dynamics, i.e. omitting the haptotactic drift term; (C) adding the therapeutic term, simulation of the effects of this term on the tumor evolution.

Figure 11 shows the comparison in case (A) of the tumor evolution over time with the three different fiber distribution functions, in absence of therapeutic strategy. In particular, the three columns refer to three different time steps: the solution is shown after 40 days, 80 days and 120 days. It is possible to observe some similarity between the tumor dynamics shown in the three rows, especially, as expected, in terms of qualitative trend of the solution and, mostly between the Peanut distribution (upper row) and the ODF (last row) cases, in terms of displacement of the cells in the tissue. Anyway, this last one is able to better capture the anisotropic pattern of the tumor evolution arising from the underlying tissue structure, avoiding the slight smoothness that the isotropic component in the tensor D_T (31), obtained with the Peanut distribution, determines in the dynamics.

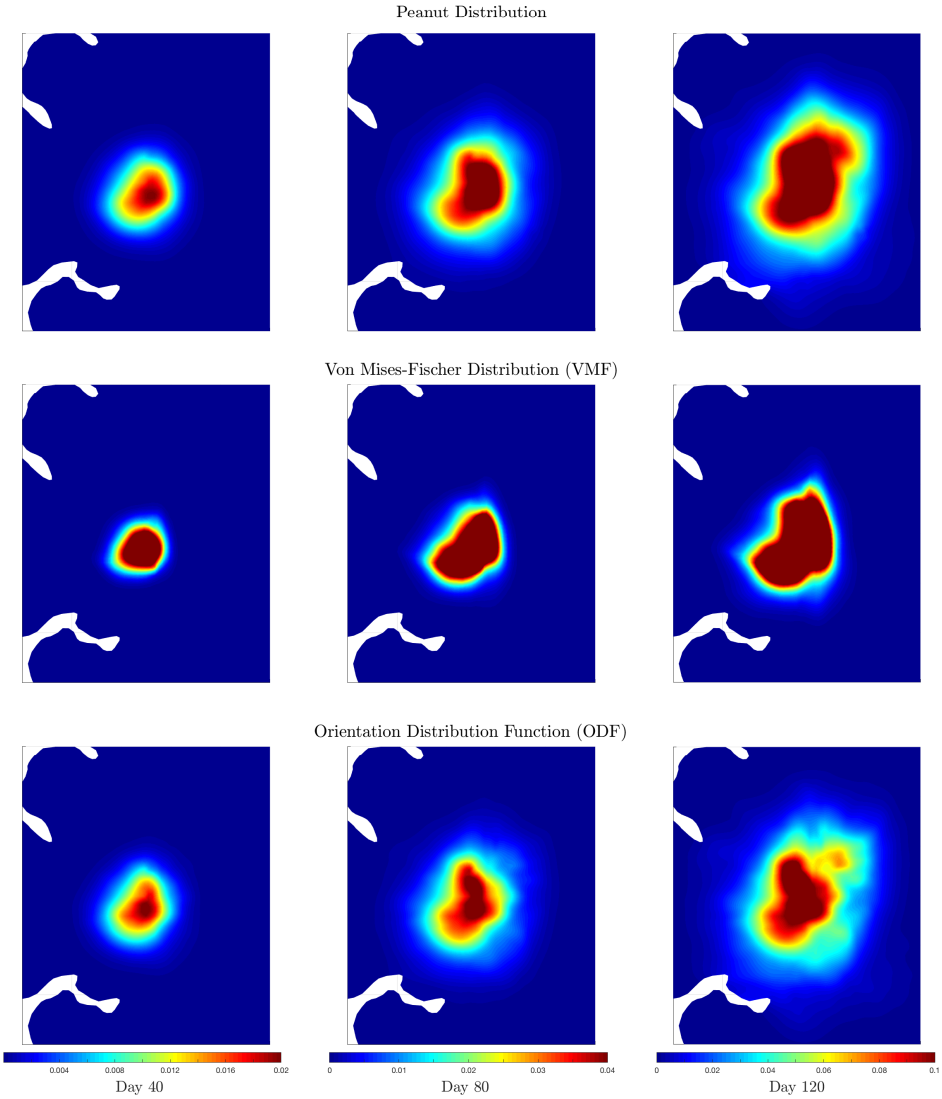

Figure 11: (A) Simulation of the evolution equation, without therapy, with the three different choices for the fiber distribution function.

Considering, then, the ODF for the description of the fiber distribution, in Figure 12 we illustrate the case (B), i.e. the numerical simulations of the tumor evolutionary equation (29) without therapy and of the same model without the advective term. This term originates from the subcellular dynamics and involves also an additional part related to the divergence of the anisotropic tumor diffusion tensor. Significant anisotropic behaviours, that are evident in the simulations of the model with advection (second row), cannot be reproduced by the pure diffusive model (first row). The tumor evolution still shows the influence of the anisotropic diffusion tensor in driving the cell movements preferentially along the fiber tracts, but with an overestimation of the tumor spread, while the haptotactic drift leads to more branched structures, that can actually be observed in clinical imaging

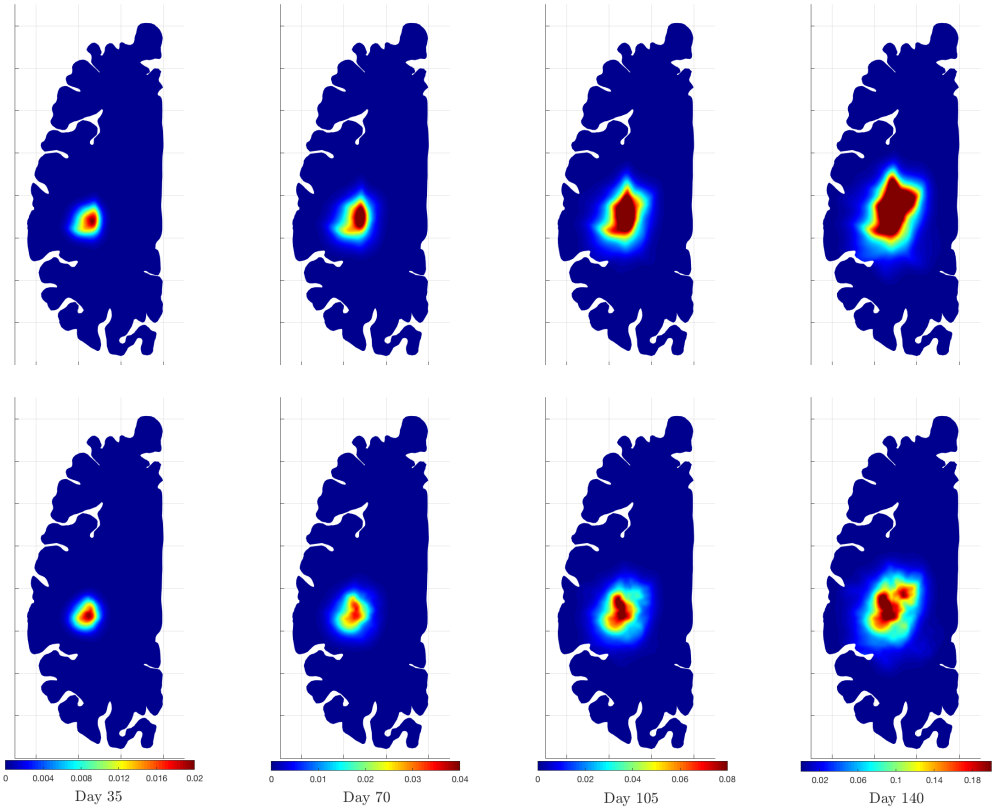

Figure 12: (B) Simulation of the pure diffusion model (first row) and of the advection-diffusion model (second row) with the ODF for the fiber description.

(see e.g., [71, 72]).
The driven motion of the cells along the tissue structure can be better observed in Figure 13, where the leading eigenvector of the tumor diffusion tensor $D_T(x)$ is also plotted, enhancing the alignment characteristics of the brain tissue and its influence on the tumor dynamics. The diffusion in both cases is anisotropic, due to the presence of the spatial-dependent coefficient $D_T(x)$ in the diffusion term, and, along the main fiber tracts, it seems to be similarly fast, but slightly faster and over-estimated in the pure-diffusion case. However, the cells in the pure diffusive model seem to be slower or less able to change direction and adapt to the tissue, especially in the region with crossing fiber, unable to reproduce branched patterns and more heterogenous distribution of the tumor density on the domain.

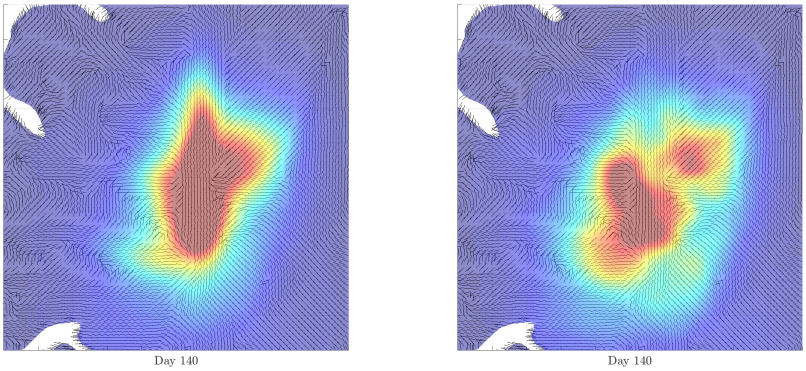

Figure 13: Tumor evolution after 140 days in the case of the no-advection model (left plot) and the advection-diffusion model (right plot), together with the fiber direction.

Finally, we test our model with a standard therapeutic strategy used in the case of newly diagnosed malignant

glioma, based on a combination of chemotherapy and radiotherapy for a period of 6 weeks. In particular, radiotherapy at a dose $d_r = 2$ Gy per fraction will be given once per day, 5 days per week from weeks 1 to 6, with a total dose of 60 Gy, while chemotherapeutic agents at a normalized dose of $d_c = 5.0$ [41] will be administered once per day from weeks 1 to 6. Analogous strategies find their motivation in different reported trials (see, e.g. trials NCT00705198 and NCT00689221 provided at https://clinicaltrials.gov).
As initial condition for the simulation with the modelled therapy we consider the tumor density obtained from the model without therapy after 5 weeks. We first observe the effect of the chemoterapy as unique applied strategy, setting the dose $d_r = 0$. Results are shown in Figure 14. In particular we consider the difference between the solution behaviour for the model without any therapeutic treatment and the one with chemotherapy. Since the chemotherapy is not aimed at killing cells, there are no changes in the tumor mass, but only in the spreading of the cells inside the tissue. Cells now, in fact, are less invasive than in the no-therapy case, since the chemotherapy is aimed to reduces cells mobility, showing a minor spreading in the tissue and a major concentration in the points closer to the initial location. In particular, in Figure 14 also the main fiber direction is shown. What emerges is that the cells, when chemotherapy is considered, tend to remain more concentrate in the area of high alignment of the fiber and they are less able to change direction and to spread inside the brain, due to the effect of the therapy on the integrin/ECM bounding.

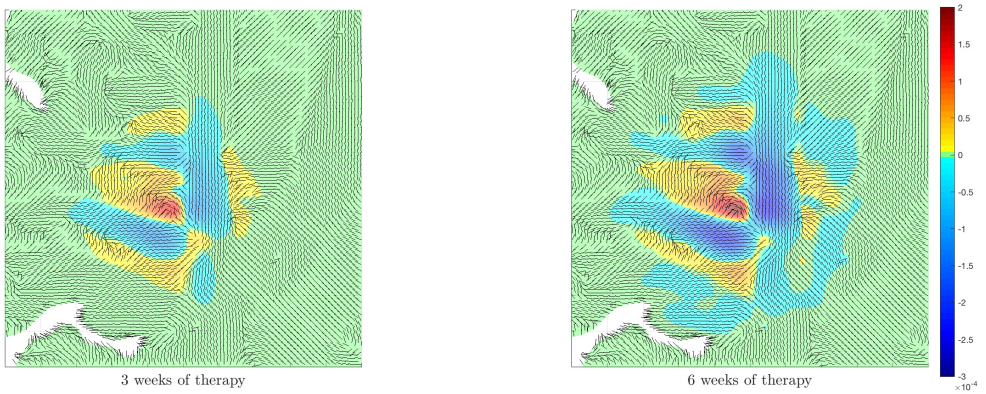

3 weeks of therapy 6 weeks of therapy

Figure 14: Difference between the tumor density in the no-therapy model and the density in the case of chemotherapy. This difference is plotted together with the fiber direction.

As last test we add also the effect of radiotherapy that, as above explained, is aimed at killing cells directly. The results are shown in Figure 15, where the difference in the cell density between the model without any therapy and the complete model with both chemo- and radio-therapy is considered. In particular, it is possible to notice at the end of the treatment a reduction in the tumor density with respect to the situation 3 weeks before (highlighted by larger areas of positive difference) especially where, due to the chemotherapy effects observed in Figure 14, the cells are more concentrated (blue areas of Figure 14).

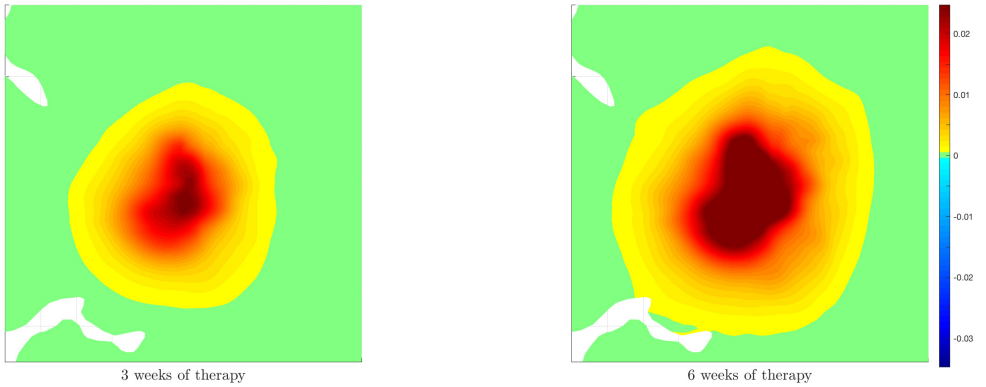

3 weeks of therapy 6 weeks of therapy

Figure 15: Difference in the tumor evolution between the no-therapy model and the case in which chemo- and radiotherapy are considered.

5 Conclusion and Perspectives

In this work we proposed a DTI-based multiscale model aiming to describe the growth, spread and invasion of glioma in the human brain. Starting from previous multiscale setting, we present an extension of them, integrating in a single model the mesoscopic description of tumor proliferation, firstly proposed by [43, 37], and a specific therapeutic approach that includes more recent ideas of drugs aimed at inhibiting cell-tissue attachment, as proposed in [41].
Moreover, the novelty here is the extensive focus on the role of the fiber structure description on the tumor evolution. In fact, the macroscopic equation for the tumor cell density, that we deduce from the mesoscale with a parabolic scaling argument, carries in its coefficient functions the information from the microscopic level. In particular, through the fiber distribution function $q(x, \theta)$, it allows to involve at the highest level of description the real data about the brain structure.
The way in which the fiber distribution function translates the original DTI information into the simulated model, together with the degree of reliability of the processed data in reproducing this information with respect to the chosen function $q(x, \theta)$, has been largely discussed. The specific capabilities of the three most used fiber distribution functions found in literature (Peanut, VMF and ODF) is investigated in details. Their strengths and their weakness, in terms of both reliability of their outputs, biological meaningfulness of the involved parameters and computational cost, have been commented in Section 3. In particular, for our purpose, the Orientation Distribution Function (24) has been chosen for the simulations. In fact, ODF better represents the influence of the fibers on the tumor migration and invasion, even though the related computational cost and complexity, with respect to the Peanut distribution (22) and the VMF distribution (23), is higher.
The simulations show, in fact, how the different choices of this function can influence the results, in terms of extension of the neoplastic area, shape, tumor infiltration and emergence of heterogenous patterns (see Figure 12). The role of the fiber in guidance the cells movement and glioma invasion in the brain tissue clearly emerges, as shown, for example, in Figure 13. At the same time, analogously to what observed also in other multiscale modelling sets [42, 36, 37], the numerical results highlight the importance of including the microscopic dynamics. In fact, the haptotactic drift term, originating from them, allows to the emergence of more prominent anisotropic behaviour, reflecting what is often observed clinically.
In addition, considering different scales allows us to include different treatment modelling, whose resulting output on the tumor invasion and migration in the tissue are clearly shown in Figures 14 and 15.
The availability of the best possible tool to translate the input data into the simulated model, as well as the possibility of extracting from these data realistic information about the computational domain, are key points towards the application of this procedure on a patient-specific model [30].
In particular, the optimal way to validate the results related to the fiber distribution choice would be the comparison of the tumor evolution over time, obtained by one of the three proposed functions $q(x, \theta)$, with clinical patient data following-up the evolution of the tumor. This remains a future task we would like to achieve since, at this moment, only data for healthy brain structure are available. The acquisition of such data, in fact, presents various difficulties, mainly related to the really poor prognosis of this disease, often discovered already at a late stage of progression.

We have focused on the role of the nervous fiber in facilitating and sustaining glioma invasive spread, in order to explore in depth the impact of this specific interaction. However more complex models, involving several other important factors, could be formulated, even though they could result much more mathematically and computationally challenging.
We underlie and stress the role of the fibers on the tumor development, mainly considering the effect of the tissue structure on the tumor invasion. Including an evolutionary equation to describe also the changes in the healthy tissue structure, due to glioma progression, would be a additional step in this direction. In fact, there is a mutual influence between neoplastic and normal tissue. The ECM structure drives tumor invasion in the brain, but also the tumor degrades the brain ECM through particular enzymes called proteases, in order to make its way inside it. In particular, recent studies are showing the possible actions of these enzymes as chemotactic forces, driving the cell movements together with the haptotactic ones. The inclusion of such a chemotaxis term could give a significant contribution to the investigation of this phenomenon.
In the same multiscale framework, the use of another scaling (different from the parabolic one) from the mesoscale to the macroscale is also an interesting direction of research. We would expect a slightly different trend in the tumor evolution with a major stress on the role of the advection term; it would be interesting to observe how, in this case, the response of the three different distributions differs from the results presented here.

Acknowledgments

The authors thank Prof. Luigi Preziosi for his suggestions and helpful discussions that initiated this work.
The authors also thank Dr. Marian Gomez Beldarrain from the Department of Neurology at the Galdakao-Usansolo Hospital for the DTI data.
This research is supported by the Basque Government through the BERC 2018- 2021 program and by the Spanish State Research Agency through BCAM Severo Ochoa excellence accreditation SEV-2017-0718 and through project RTI2018- 093416-B-I00 funded by (AEI/FEDER, UE) and acronym "MULTIQUANT".
This project has received funding from the European Union's Horizon 2020 research and innovation programme under the Marie Skłodowska-Curie grant agreement No. 713673. The project that gave rise to these results received the support of a fellowship from "la Caixa" Foundation (ID 100010434). The fellowship code is LCF/BQ/IN17/11620056.
This work was performed also in the frame of the activities sponsored by the National Group of Mathematical Physics (GNFM-INdAM) and by the University of Parma (Italy).

References

[1] Wrensch, M., Minn, Y., Chew, T., Bondy, M., & Berger, M. S. (2002). Epidemiology of primary brain tumors: current concepts and review of the literature. *Neuro-oncology*, **4(4)**, 278-299.

[2] G. Gritsenko, P., Ilina, O., & Friedl, P. (2012). Interstitial guidance of cancer invasion. *The Journal of pathology*, **226(2)**, 185-199.

[3] Giovanna, M. D., & Kaye, A. H. (2007). Integrins: molecular determinants of glioma invasion. *Journal of clinical neuroscience*, **14(11)**, 1041-1048.

[4] Demuth, T., & Berens, M. E. (2004). Molecular mechanisms of glioma cell migration and invasion. *Journal of neuro-oncology*, **70(2)**, 217-228.

[5] Huttenlocher, A., & Horwitz, A. R. (2011). Integrins in cell migration. *Cold Spring Harbor perspectives in biology*, **3(9)**, a005074.

[6] Hatzikirou, H., Deutsch, A., Schaller, C., Simon, M., & Swanson, K. (2005). Mathematical modelling of glioblastoma tumour development: a review. *Mathematical Models and Methods in Applied Sciences*, **15(11)**, 1779-1794.

[7] Martirosyan, N. L., Rutter, E. M., Ramey, W. L., Kostelich, E. J., Kuang, Y., & Preul, M. C. (2015). Mathematically modeling the biological properties of gliomas: a review. *Mathematical Biosciences & Engineering*, **12(4)**, 879-905.

[8] Alfonso, J. C. L., Talkenberger, K., Seifert, M., Klink, B., Hawkins-Daarud, A., Swanson, K. R., ... & Deutsch, A. (2017). The biology and mathematical modelling of glioma invasion: a review. *Journal of the Royal Society Interface*, **14(136)**, 20170490.

[9] Hatzikirou, H., Basanta, D., Simon, M., Schaller, K., & Deutsch, A. (2012). 'Go or grow': the key to the emergence of invasion in tumour progression?. *Mathematical medicine and biology: a journal of the IMA*, **29(1)**, 49-65.

[10] Böttger, K., Hatzikirou, H., Chauviere, A., & Deutsch, A. (2012). Investigation of the migration/proliferation dichotomy and its impact on avascular glioma invasion. *Mathematical Modelling of Natural Phenomena*, 7(1), 105-135.

[11] Gevertz, J. L., & Torquato, S. (2006). Modeling the effects of vasculature evolution on early brain tumor growth. *Journal of Theoretical Biology*, **243(4)**, 517-531.

[12] Tanaka, M. L., Debinski, W., & Puri, I. K. (2009). Hybrid mathematical model of glioma progression. *Cell proliferation*, 42(5), 637-646.

[13] Kim, Y., & Roh, S. (2013). A hybrid model for cell proliferation and migration in glioblastoma. *Discrete & Continuous Dynamical Systems-B*, **18(4)**, 969-1015.

[14] Swanson, K. R., Alvord Jr, E. C., & Murray, J. D. (2000). A quantitative model for differential motility of gliomas in grey and white matter. *Cell proliferation*, **33(5)**, 317-329.

[15] Jbabdi, S., Mandonnet, E., Duffau, H., Capelle, L., Swanson, K. R., Pélégrini-Issac, M., ... & Benali, H. (2005). Simulation of anisotropic growth of low-grade gliomas using diffusion tensor imaging. *Magnetic Resonance in Medicine: An Official Journal of the International Society for Magnetic Resonance in Medicine*, **54(3)**, 616-624.

[16] Clatz, O., Sermesant, M., Bondiau, P. Y., Delingette, H., Warfield, S. K., Malandain, G., & Ayache, N. (2005). Realistic simulation of the 3-D growth of brain tumors in MR images coupling diffusion with biomechanical deformation. *IEEE transactions on medical imaging*, **24(10)**, 1334-1346.

[17] Konukoglu, E., Clatz, O., Bondiau, P. Y., Delingette, H., & Ayache, N. (2010). Extrapolating glioma invasion margin in brain magnetic resonance images: suggesting new irradiation margins. *Medical image analysis*, **14(2)**, 111-125.

[18] Cobzas, D., Mosayebi, P., Murtha, A., & Jagersand, M. (2009). Tumor invasion margin on the riemannian space of brain fibers. In *International Conference on Medical Image Computing and Computer-Assisted Intervention*, pp. 531-539. Springer, Berlin, Heidelberg.

[19] Swanson, K. R., Alvord Jr, E. C., & Murray, J. D. (2003). Virtual resection of gliomas: effect of extent of resection on recurrence. *Mathematical and Computer Modelling*, **37(11)**, 1177-1190.

[20] Swanson, K. R., Rostomily, R. C., & Alvord Jr, E. C. (2008). A mathematical modelling tool for predicting survival of individual patients following resection of glioblastoma: a proof of principle. *British journal of cancer*, **98(1)**, 113.

[21] Wang, C. H., Rockhill, J. K., Mrugala, M., Peacock, D. L., Lai, A., Jusenius, K., ... & Alvord, E. C. (2009). Prognostic significance of growth kinetics in newly diagnosed glioblastomas revealed by combining serial imaging with a novel biomathematical model. *Cancer research*, **69(23)**, 9133-9140.

[22] Chaplain, M. A., & Lolas, G. (2006). Mathematical modelling of cancer invasion of tissue: dynamic heterogeneity. *Networks and Heterogenous Media*, **1(3)**, 399-439.

[23] Anderson, A. R., Chaplain, M. A., Newman, E. L., Steele, R. J., & Thompson, A. M. (2000). Mathematical modelling of tumour invasion and metastasis. *Computational and mathematical methods in medicine*, **2(2)**, 129-154.

[24] Bondiau, P. Y., Clatz, O., Sermesant, M., Marcy, P. Y., Delingette, H., Frenay, M., & Ayache, N. (2008). Biocomputing: numerical simulation of glioblastoma growth using diffusion tensor imaging. *Physics in Medicine & Biology*, **53(4)**, 879.

[25] Barocas, V. H., & Tranquillo, R. T. (1997). An anisotropic biphasic theory of tissue-equivalent mechanics: the interplay among cell traction, fibrillar network deformation, fibril alignment, and cell contact guidance. *Journal of biomechanical engineering*, **119(2)**, 137-145.

[26] Maini, P. K. (1989). Spatial and spatio-temporal patterns in a cell-haptotaxis model. *Journal of mathematical biology*, **27(5)**, 507-522.

[27] Tosin, A., & Preziosi, L. (2010). Multiphase modeling of tumor growth with matrix remodeling and fibrosis. *Mathematical and Computer Modelling*, **52(7-8)**, 969-976.

[28] Ambrosi, D., & Preziosi, L. (2002). On the closure of mass balance models for tumor growth. *Mathematical Models and Methods in Applied Sciences*, **12(05)**, 737-754.

[29] Colombo, M. C., Giverso, C., Faggiano, E., Boffano, C., Acerbi, F., & Ciarletta, P. (2015). Towards the personalized treatment of glioblastoma: integrating patient-specific clinical data in a continuous mechanical model. *PLoS One*, **10(7)**, e0132887.

[30] Agosti, A., Cattaneo, C., Giverso, C., Ambrosi, D., & Ciarletta, P. (2018). A computational framework for the personalized clinical treatment of glioblastoma multiforme. *ZAMM-Journal of Applied Mathematics and Mechanics/Zeitschrift für Angewandte Mathematik und Mechanik*, **98(12)**, 2307-2327.

[31] Hillen, T. (2006). M^5 mesoscopic and macroscopic models for mesenchymal motion. *Journal of mathematical biology*, **53(4)**, 585-616.

[32] Hillen, T., & Painter, K. J. (2013). Transport and anisotropic diffusion models for movement in oriented habitats. In *Dispersal, individual movement and spatial ecology* (pp. 177-222). Springer, Berlin, Heidelberg.

[33] Bellomo, N., Bellouquid, A., Nieto, J., & Soler, J. (2012). On the asymptotic theory from microscopic to macroscopic growing tissue models: An overview with perspectives. *Mathematical Models and Methods in Applied Sciences*, **22(01)**, 1130001.

[34] Chauviere, A., Hillen, T., & Preziosi, L. (2007). Modeling cell movement in anisotropic and heterogeneous network tissues. *Networks and heterogeneous media*, **2(2)**, 333.

[35] Meral, G., Stinner, C., & Surulescu, C. (2015) On a multiscale model involving cell contractivity and its effects on tumor invasion. *Discrete & Continuous Dynamical Systems - B*, **20(1)**,189-213.

[36] Engwer, C., Hillen, T., Knappitsch, M., & Surulescu, C. (2015). Glioma follow white matter tracts: a multiscale DTI-based model. *Journal of Mathematical Biology*, **71**, 551-582.

[37] Engwer, C., Hunt, A., Surulescu, C. (2016) Effective equations for anisotropic glioma spread with proliferation: a multiscale approach and comparisons with previous settings. *Mathematical Medicine and Biology*, **33**, 435-459.

[38] Lorenz, T., & Surulescu, C. (2014). On a class of multiscale cancer cell migration models: Well-posedness in less regular function spaces. *Mathematical Models and Methods in Applied Sciences*, **24(12)**, 2383-2436.

[39] Kelkel, J., & Surulescu, C. (2012). A multiscale approach to cell migration in tissue networks. *Mathematical Models and Methods in Applied Sciences*, **22(03)**, 1150017.

[40] Stinner, C., Surulescu, C., & Winkler, M. (2014). Global weak solutions in a PDE-ODE system modeling multiscale cancer cell invasion. *SIAM Journal on Mathematical Analysis*,**46(3)**, 1969-2007.

[41] Hunt, A., & Surulescu, C. (2017). A multiscale modeling approach to glioma invasion with therapy. *Vietnam Journal of Mathematics*, **45(1-2)**, 221-240.

[42] Engwer, C., Knappitsch, M., & Surulescu, C. (2016). A multiscale model for glioma spread including cell-tissue interactions and proliferation. *Mathematical Biosciences & Engineering*, **13(2)**, 443-460.

[43] Bellomo, N., Bellouquid, A., Nieto, J., & Soler, J. (2010). Complexity and mathematical tools toward the modelling of multicellular growing systems. *Mathematical and Computer Modelling*, **51(5-6)**, 441-451.

[44] Chicoine, M. R., & Silbergeld, D. L. (1995). Assessment of brain tumor cell motility in vivo and in vitro. *Journal of neurosurgery*, **82(4)**, 615-622.

[45] Giese, A., Bjerkvig, R., Behrens, M. E., & Westphal, M. (2003) Cost of migration: invasion of malignant gliomas and implications for treatment. *Journal of Clinical Oncology* **21**, 1624–1636.

[46] Rockne, R., Alvord, E. C., Rockhill, J. K., & Swanson, K. R. (2009). A mathematical model for brain tumor response to radiation therapy. *Journal of mathematical biology*, **58(4-5)**, 561.

[47] Lefrank, F., Brotchi, J., & Kiss, R. (2005) Possible future issues in the treatment of glioblastomas: special emphasis on cell migration and the resistance of migrating glioblastoma cells to apoptosis. *Journal of Clinical Oncology* **23**, 2411-2422.

[48] Sachs, R. K., Hlatky, L. R., & Hahnfeldt, P. (2001) Simple ODE models of tumor growth and anti-angiogenic or radiation treatment. *Mathematical and Computer Modelling*, **33(12-13)**, 1297-1305.

[49] Sun, S., Titushkin, I., & Cho, M. (2006). Regulation of mesenchymal stem cell adhesion and orientation in 3D collagen scaffold by electrical stimulus. *Bioelectrochemistry*, **69(2)**, 133-141.

[50] Othmer, H. G., & Hillen, T. (2000). The diffusion limit of transport equations derived from velocity-jump processes. *SIAM Journal on Applied Mathematics*, **61(3)**, 751-775.

[51] Ruzicka, M. (2006). *Nichtlineare Funktionalanalysis: Eine Einführung*. Springer-Verlag.

[52] Showalter, R. E. (2013). *Monotone operators in Banach space and nonlinear partial differential equations* (Vol. 49). American Mathematical Soc.

[53] Fangliang, D. (2012). Maximum Principle and Application of Parabolic Partial Differential Equations. *IERI Procedia*, **3**, 198-205.

[54] Kingsley, P. B., & Monahan, W. G. (2005). Contrast-to-noise ratios of diffusion anisotropy indices. *Magnetic Resonance in Medicine: An Official Journal of the International Society for Magnetic Resonance in Medicine*, **53(4)**, 911-918.

[55] Papadakis, N. G., Xing, D., Houston, G. C., Smith, J. M., Smith, M. I., James, M. F., ... & Carpenter, T. A. (1999). A study of rotationally invariant and symmetric indices of diffusion anisotropy. *Magnetic resonance imaging*, **17(6)**, 881-892.

[56] Hasan, K. M., Alexander, A. L., & Narayana, P. A. (2004). Does fractional anisotropy have better noise immunity characteristics than relative anisotropy in diffusion tensor MRI? An analytical approach.*Magnetic Resonance in Medicine: An Official Journal of the International Society for Magnetic Resonance in Medicine*, **51(2)**, 413-417.

[57] Painter, K. J., & Hillen, T. (2013). Mathematical modelling of glioma growth: the use of diffusion tensor imaging (DTI) data to predict the anisotropic pathways of cancer invasion. *Journal of theoretical biology*, **323**, 25-39.

[58] Basser, P. J. (2008). Diffusion and diffusion tensor MR imaging: fundamentals. *Magnetic resonance imaging of the brain and spine*,1752-1767.

[59] Mardia, K. V., & Jupp, P. E. (2009). *Directional statistics* (Vol. 494). John Wiley & Sons.

[60] Aganj, I., Lenglet, C., Sapiro, G., Yacoub, E., Ugurbil, K., & Harel, N. (2010). Reconstruction of the orientation distribution function in single-and multiple-shell q-ball imaging within constant solid angle. *Magnetic resonance in medicine*, **64(2)**, 554-566.

[61] Aganj, I., Lenglet, C., Jahanshad, N., Yacoub, E., Harel, N., Thompson, P. M., & Sapiro, G. (2011). A Hough transform global probabilistic approach to multiple-subject diffusion MRI tractography. *Medical image analysis*, **15(4)**, 414-425.

[62] Perrin, M., Poupon, C., Rieul, B., Leroux, P., Constantinesco, A., Mangin, J. F., & LeBihan, D. (2005). Validation of q-ball imaging with a diffusion fibre-crossing phantom on a clinical scanner. *Philosophical Transactions of the Royal Society B: Biological Sciences*, **360(1457)**, 881-891.

[63] Bloy, L., & Verma, R. (2008). On computing the underlying fiber directions from the diffusion orientation distribution function. In *International Conference on Medical Image Computing and Computer-Assisted Intervention* (pp. 1-8). Springer, Berlin, Heidelberg.

[64] Tuch, D. S., Reese, T. G., Wiegell, M. R., & Wedeen, V. J. (2003). Diffusion MRI of complex neural architecture. *Neuron*, **40(5)**, 885-895.

[65] Jenkinson, M., Beckmann, C. F., Behrens, T. E., & Woolrich, M. W. (2012). Smith SM. Fsl. *Neuroimage*, **62**, 782-90.

[66] Sidani, M., Wessels, D., Mouneimne, G., Ghosh, M., Goswami, S., Sarmiento, C., ... & Eddy, R. (2007). Cofilin determines the migration behavior and turning frequency of metastatic cancer cells. *The Journal of cell biology*, **179(4)**, 777-791.

[67] Mercapide, J., Lopez De Cicco, R., Castresana, J. S., & Klein-Szanto, A. J. (2003). Stromelysin-1/matrix metalloproteinase-3 (MMP-3) expression accounts for invasive properties of human astrocytoma cell lines. *International journal of cancer*, **106(5)**, 676-682.

[68] Besserer, J., & Schneider, U. (2015). Track-event theory of cell survival with second-order repair. *Radiation and environmental biophysics*, **54(2)**, 167-174.

[69] Fischl, B. (2012). FreeSurfer. *Neuroimage*, **62(2)**, 774-781.

[70] Geuzaine, C., & Remacle, J. F. (2009). Gmsh: A 3-D finite element mesh generator with built-in pre-and post-processing facilities. *International journal for numerical methods in engineering*, **79(11)**, 1309-1331.

[71] Zinn, P. O., Majadan, B., Sathyan, P., Singh, S. K., Majumder, S., Jolesz, F. A., & Colen, R. R. (2011). Radiogenomic mapping of edema/cellular invasion MRI-phenotypes in glioblastoma multiforme. *PloS one*, **6(10)**, e25451.

[72] Gerstner, E. R., Chen, P. J., Wen, P. Y., Jain, R. K., Batchelor, T. T., & Sorensen, G. (2010). Infiltrative patterns of glioblastoma spread detected via diffusion MRI after treatment with cediranib. *Neuro-oncology*, **12(5)**, 466-472.

A Appendix

A.1 Diffusion Anisotropy Indices

Considering a general tensor D, with eigenvalues $\lambda_1 \geq \lambda_2 \geq \lambda_3$ and average $\bar{\lambda} = \frac{\lambda_1+\lambda_2+\lambda_3}{3}$, several scalar indices have been proposed in literature [55, 56, 57] to characterize its anisotropy. They are called *diffusion anisotropy indices* (DAI) and, among them, we recall:

- RA, *relative anisotropy*, defined as $RA = \dfrac{\sqrt{(\lambda_1-\bar{\lambda})^2+(\lambda_2-\bar{\lambda})^2+(\lambda_3-\bar{\lambda})^2}}{\sqrt{6}\bar{\lambda}}$, representing the ratio of the anisotropic part of the diffusion tensor to its isotropic part;
- FA, *fractional anisotropy*, defined as $FA = \sqrt{\dfrac{3}{2}}\dfrac{\sqrt{(\lambda_1-\bar{\lambda})^2+(\lambda_2-\bar{\lambda})^2+(\lambda_3-\bar{\lambda})^2}}{\sqrt{\lambda_1^2+\lambda_2^2+\lambda_3^2}}$, reflecting the fraction of the magnitude of the diffusion tensor that can be ascribed to anisotropic diffusion;
- VR, *volume ratio*, defined as $VR = \dfrac{\lambda_1\,\lambda_2\,\lambda_3}{\bar{\lambda}^3}$, representing the ratio of the ellipsoid volume to the volume of a sphere of radius $\bar{\lambda}$.

These three indices are characterized by: rotational invariance, i.e. there is no bias due to fiber orientation in estimating the anisotropy; symmetry respect to the three principal diffusivities, i.e. sorting -independency and less sensitivity to extraneous noise.
Different studies [54, 55, 56] have shown that there are significant differences between these three indices, especially in terms of sensitivity to anisotropy, contrast between low and high anisotropy areas and contrast-to-noise ratio. However, these differences are not so strong, especially for small anisotropy variation, to justify an intrinsic advantage of one index on the others.
In particular, FA seems to provide the most detailed representation of the anisotropy characterizing the tissue; it reveals well the various anisotropic structures, even for area of mild and low anisotropy, providing good anatomical details of the anisotropic regions, although it has an increasing noise in the area of low anisotropy.

A.2 Peanut distribution

Firstly introduced by Painter and Hillen in [57], the definition of the Peanut distribution is related to the concept of apparent diffusion coefficient (ADC). It is defined, generally, by taking the ratio of the mean-squared displacement measured along a particular direction and the diffusion time of the experiment.
In the specific case of a simple model for anisotropic diffusion, described by a diffusion tensor D, the mean-squared displacement along a given direction $\theta \in \mathbb{S}^{n-1}$ is given by $\sigma_\theta^2 = 2t\,\theta^T D\,\theta$, where t is the diffusion time. So, ADC in the direction θ is given by the following expression [58]

$$ADC_\theta := \frac{\sigma_\theta^2}{2t} = \theta^T D\,\theta\,.$$

Since ADC is an indicator of the anisotropy of the tissue, a possible choice for the construction of the fiber distribution function is to assume that the cell turning is directly correlated to it. As a consequence, the Peanut distribution function for the fiber orientation description takes the following form:

$$q(x,\theta) = \frac{n}{|\mathbb{S}^{n-1}|Tr\,(D_W(x))}\theta^T D_W(x)\theta\,. \tag{30}$$

Following Lemma 1 in [57] it is possible to get the general expression for the tumor diffusion tensor $D_T(x)$ in n dimension, starting from the relation (16):

$$D_T(x) = \frac{s^2}{(n+2)\lambda_0}\left(\mathbb{I} + \frac{2}{Tr(D_W)}D_W\right). \tag{31}$$

This expression reveals the direct link between the original tensor D_W and the macroscopic diffusion tensor D_T, presenting an isotropic component proportional to $\mathbb{I}$ and an anisotropic component proportional to D_W. So, theoretically, even in case of completely anisotropic environment, D_T will always present an isotropic part, leading to a partial lost of the data information.

A.3 Von Mises-Fisher Distribution

The Von Mises-Fisher (VMF) distribution is one of the most useful distribution for spherical data from the standpoint of the statistical inference, as largely explain in [59].
The most general expression of this distribution for data on $\mathbb{S}^{n-1}$ results in a probability density function of this form:

$$f(\mathbf{x}, \mu, \kappa) = \left(\frac{\kappa}{2}\right)^{\frac{n}{2}-1} \frac{1}{\Gamma(\frac{n}{2})\mathrm{I}_{\frac{n}{2}-1}} \exp\{\kappa \mu^T \mathbf{x}\}$$

where $\kappa \geq 0$ is the concentration parameter, μ is the mean direction, with norm one, I_ν is the modified Bessel function of the first kind and of order ν and Γ is the Gamma function.
This distribution, for $\kappa > 0$, has a mode at the mean direction and, the larger the value of the concentration parameter, the greater the clustering around this direction.
The special cases which we are interesting in are defined for $n = 2$ (planar case) and $n = 3$ (spherical case).

Consider the following representation of the water diffusion tensor D_W:

$$D_W(x) = \sum_{i=1}^{n} \lambda_i(x)\phi_i(x)\phi_i(x)^T$$

with λ_i and ϕ_i, for $i = 1...n$, respectively eigenvalues and corresponding eigenvectors of the tensor, orthogonal and normalized due to its symmetry; in particular, the eigenvectors denote the axis of dominating anisotropy and the eigenvalues the degree of anisotropy.

With this notation, for the planar case, the dominant direction μ for the movement is given by the leading eigenvector of D_W, because is natural to consider that the turning is concentrated in the dominant direction of anisotropy [57]. Additionally, two other requirements are considering for building the well-known and used expression introduced in [57]. Firstly a constant parameter $\delta \in [0, 1]$, describing an inherent degree of randomised turning, is add for partially controlling the size of the resulting isotropic component of D_T. Then the concentration parameter κ is substituted by a function $k(x)$ for the concentration level that should increase along the direction of greater anisotropy. For this reason a possible choice for $k(x)$ consists in considering it proportional to the fractional anisotropy of D_W through a concentration factor κ, describing the sensitivity of the cells to the directional information given by the environment, i.e. $k(x) = \kappa FA(D_W(x))$.
Thus, considering a bimodal form of the VMF distribution, the expression for the fiber distribution function results:

$$q(x, \theta) = \frac{\delta}{2\pi} + (1-\delta)\frac{1}{4\pi \mathrm{I}_0(k)} \left(e^{k(x)\phi_1 \cdot \theta} + e^{-k(x)\phi_1 \cdot \theta}\right). \tag{32}$$

Considering (16) and (32), the expression of $D_T(x)$ for $n = 2$, as explicitly calculated into [32], is given by:

$$D_T(x) = \frac{s^2}{2\lambda_0}\left(\left(\delta + (1-\delta)\left(1 - \frac{\mathrm{I}_2(k(x))}{\mathrm{I}_0(k(x))}\right)\right)\mathbb{I} + 2(1-\delta)\frac{\mathrm{I}_2(k(x))}{\mathrm{I}_0(k(x))}\phi_1(x)\phi_1(x)^T\right). \tag{33}$$

In particular, we observe that the parameter δ plays the role of weight for the isotropic and the anisotropic component of D_T, determining the relevance of each part; analogous role is played by the function $k(x)$. If $\delta = 1$, D_T simply describes a complete isotropic environment. This also happens, for the characteristics of the ratio $\frac{\mathrm{I}_2(k(x))}{\mathrm{I}_0(k(x))}$, when $k(x) = 0$, that means either the case of isotropic DTI data, i.e. $FA(D_W) = 0$, or cells not responding to the environmental anisotropy, i.e. $\kappa = 0$. On the contrary, when the value of $k(x)$ grows or the value of δ is close to zero, the anisotropic part gains more importance.

Unlike the Peanut distribution case, here it is possible to have much more control on the fiber density trend, with the theoretical possibility of no limit for the values of $FA(D_T)$, changing δ and κ.
From one side, this means that D_T may be calibrated in order to be as similar as possible to the tensor D_W, but from the other hand this makes it strongly dependent on the parameters κ and δ, which meaning and identification it is not so clear. In fact, although it seem reasonable to choose them fitting the original data, their biological interpretation and estimation remains still uncertain and, therefore, the reliability of the results may be prejudiced.
In particular we compare the effect on $FA(D_T)$ of these parameters κ and δ. The results are shown in Figure 16 for the single point case and in Figures 17 and 18 for a 2D slice.
Extending the analysis to the $n = 3$ case, following [57], we consider the bimodal form of the distribution combined with a uniform distribution depending on the parameter $\delta \in [0, 1]$. The fiber configuration in this case is described by:

$$q(x, \theta) = \frac{\delta}{4\pi} + (1-\delta)\frac{k(x)}{4\pi \sinh k(x)} \left(\cosh(k(x)\phi_1 \cdot \theta)\right). \tag{34}$$

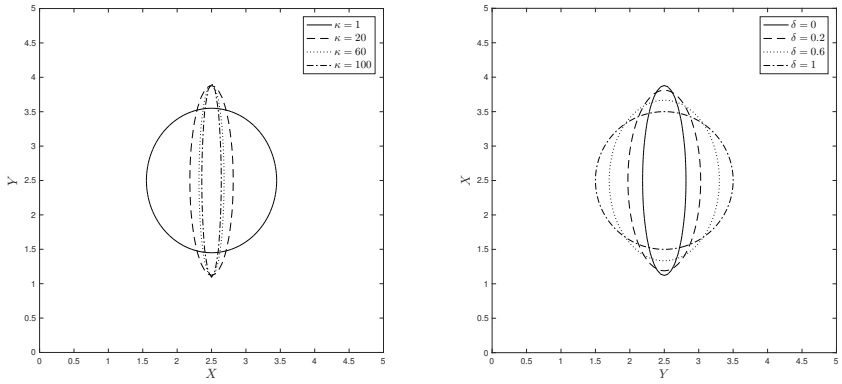

Figure 16: $D_T(\mathbf{x})$ for VMF Distribution varying κ (left) and δ (right).

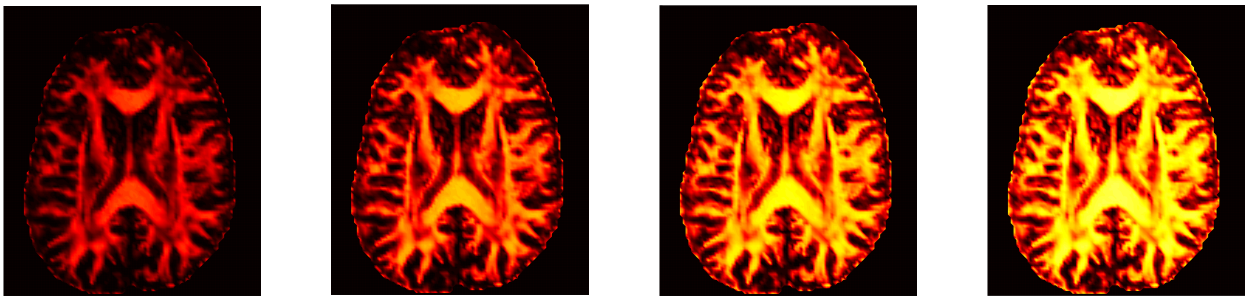

FA(D_T) for $\kappa = 3$ FA(D_T) for $\kappa = 5$ FA(D_T) for $\kappa = 7$ FA(D_T) for $\kappa = 10$

Figure 17: FA(D_T) for different values of κ and δ fixed to 0.05.

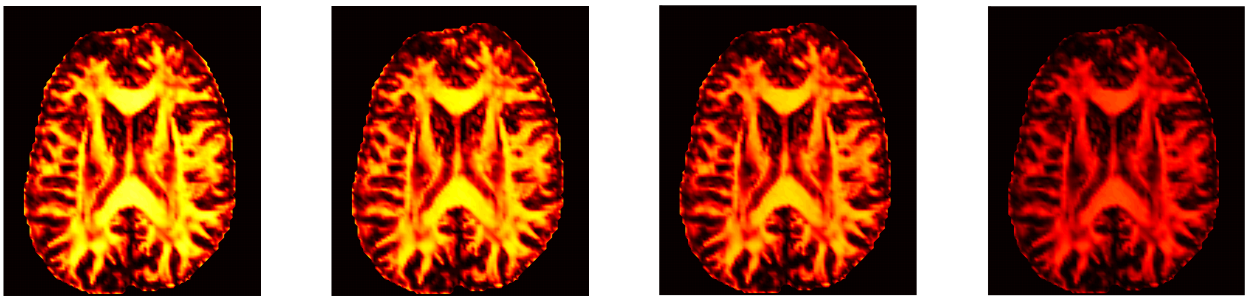

FA(D_T) for $\delta = 0.001$ FA(D_T) for $\delta = 0.05$ FA(D_T) for $\delta = 0.1$ FA(D_T) for $\delta = 0.3$

Figure 18: FA(D_T) for different values of δ and κ fixed to 7.

The direct calculation of the tumor diffusion tensor expression provides:

$$D_T(x) = \frac{s^2}{3\lambda_0}\left[\left(\delta + (1-\delta)\left(\frac{\coth k(x)}{k(x)} - \frac{1}{k(x)^2}\right)\right)\mathbb{I} + (1-\delta)\left(1 - \frac{3\coth k(x)}{k(x)} + \frac{3}{k(x)^2}\right)\phi_1(x)\phi_1(x)^T\right]. \quad (35)$$

A.4 Orientation Distribution Function

A third approach is based on the concept of Orientation Distribution Function, simply indicated as ODF. The 3D probability density function (PDF) of diffusion $\mathcal{P}(\mathbf{x}, \hat{t})d\Omega$ gives the displacement probability for a molecule in the point $\mathbf{x}$ to be located inside a fiber bundle passing in the direction $\hat{t}$ through the infinitesimal solid angle $d\Omega$, providing helpful information in the study of the tissue microstructure. The ODF, instead, represent the marginal probability of diffusion in a given direction and it is fundamental for mapping the orientation architecture of the tissue [60, 61].

Assuming that the PDF of diffusion is a symmetric function $\mathcal{P}(\vec{r}) = \mathcal{P}(-\vec{r})$ and considering the standard spherical coordinates system, the probability of diffusion in a direction $\hat{t}$ through the solid angle $d\Omega$ is computed

by integrating the displacement probabilities for all magnitude r, keeping the direction constant, i.e.

$$ODF(\hat{t}) = \int_0^\infty \mathcal{P}(r\hat{t})r^2 dr\,. \tag{36}$$

The application of this distribution to fiber orientation analysis comes from some experimental results that show the correspondence between the peaks of the ODF and the principal directions of the underlying fibers [62]. In particular a non-linear, monotonically increasing, relationship between the FA of generated diffusion tensor related to an underlying fiber and the mean principal curvature of the ODF at the principal direction of the fiber itself is shown in [63].

In the case of Diffusion Tensor Imaging [61], the probability density function of diffusion is given by the standard 3D Gaussian PDF:

$$\mathcal{P}(r\hat{t}) = \frac{1}{(2\pi)^{\frac{3}{2}}|D|^{\frac{1}{2}}} e^{-\frac{1}{2}r\hat{t}^T D^{-1} r\hat{t}}$$

with D proportional to the estimated diffusion tensor and $|D|$ denoting the determinant of this tensor .

Integrating it, following relation (36), we obtain the following expression for ODF:

$$ODF(\hat{t}) = \frac{1}{4\pi|D|^{\frac{1}{2}}(\hat{t}^T(D)^{-1}\hat{t})^{\frac{3}{2}}}\,.$$

Thus, setting the fiber orientation density $q(x,\theta)$ equal to ODF, setting the direction $\hat{t}$ equal to the angle θ and considering the water diffusion tensor D_W as original estimated tensor, we obtain:

$$q(x,\theta) = \frac{1}{4\pi|D_W(x)|^{\frac{1}{2}}(\theta^T(D_W(x))^{-1}\theta)^{\frac{3}{2}}} \tag{37}$$

In this case we do not have an explicit expression for the tumor diffusion tensor D_T, but we consider its integral formulation (16) and we approximate it numerically.